

Optics Letters

Photoacoustic elastography

PENGFEI HAI, JUNJIE YAO, GUO LI, CHIYE LI, AND LIHONG V. WANG*

Optical Imaging Laboratory, Department of Biomedical Engineering, Washington University in St. Louis, St. Louis, Missouri 63130, USA

*Corresponding author: lhwang@wustl.edu

Received 29 September 2015; revised 28 November 2015; accepted 11 January 2016; posted 13 January 2016 (Doc. ID 250984); published 5 February 2016

Elastography can noninvasively map the elasticity distribution in biological tissue, which can potentially be used to reveal disease conditions. In this Letter, we have demonstrated photoacoustic elastography by using a linear-array photoacoustic computed tomography system. The feasibility of photoacoustic elastography was first demonstrated by imaging the strains of single-layer and bilayer gelatin phantoms with various stiffness values. The measured strains agreed well with theoretical values, with an average error of less than 5.2%. Next, *in vivo* photoacoustic elastography was demonstrated on a mouse leg, where the fat and muscle distribution was mapped based on the elasticity contrast. We confirmed the photoacoustic elastography results by ultrasound elastography performed simultaneously. © 2016 Optical Society of America

OCIS codes: (170.5120) Photoacoustic imaging; (170.3880) Medical and biological imaging; (170.6935) Tissue characterization.

<http://dx.doi.org/10.1364/OL.41.000725>

Elastic properties of biological tissues can reflect pathological conditions [1,2]. Elastography, an imaging technique that is typically implemented using existing medical imaging techniques, can map the elasticity distribution in biological tissue [3]. Elastography was first performed using ultrasound imaging in 1991 [4]. Later, elastography was implemented using magnetic resonance imaging, namely, magnetic resonance elastography, at the whole body level with a spatial resolution of $\sim 1\text{--}3$ mm [5]. Elastography was also implemented in optical coherence tomography (OCT), which has greatly improved the spatial resolution to $\sim 1\text{--}10$ μm , but OCT has limited imaging depth (~ 1 mm in the skin) due to the strong optical scattering in biological tissue [6].

Photoacoustic (PA) tomography (PAT) is a hybrid imaging technique that combines rich optical absorption contrast and high ultrasonic spatial resolution [7]. PAT has proven capable of imaging anatomical, functional, molecular, and metabolic information of biological tissue [8–11]. There have been several PA studies on measuring the elastic properties of biological tissue. In one study, the viscoelasticity of biological tissues was imaged by PA technique, but the elasticity could not be measured because the detected PA signal phase delay was related to the viscosity-elasticity ratio instead of the elasticity alone [12,13]. In a second study, the volume-averaged Young's modulus of soft

tissue was measured by a PA sensing technique, which, however, possessed no spatial resolution [14]. Yet another study introduced speckles in PA images for sample displacement estimation, but demonstrated the concept only with simulation data [15]. So far, elastography has not been successfully implemented using PA imaging. Here, we demonstrate PA elastography capable of high-resolution strain imaging of biological tissue based on the contrast of Young's modulus. Implemented using photoacoustic computed tomography (PACT), PA elastography can map the mechanical contrast in biological tissue while maintaining high spatial resolution and excellent penetration depth.

PA elastography was developed based on a linear-array PACT system [16], which is capable of high-resolution imaging of the elasticity distribution in tissue *in vivo*. A 10 ns pulsed laser beam at 680 nm was used for PA excitation with a 20 Hz pulse repetition rate. Light was first coupled into a fiber bundle. The fiber bundle was then split into two rectangular light bars mounted on each side of a linear ultrasonic transducer array (LZ250, VisualSonics Inc., 21 MHz center frequency, 256 elements), which detected the generated photoacoustic waves. PA signals were sampled at 84 MHz. For each laser pulse, one quarter of the 256 ultrasonic array elements were used for detecting PA signals. Acquired with four laser pulses, the full data set was used to reconstruct a cross-sectional PA image, yielding a frame rate of 5 Hz. The spatial resolutions of the PACT system were 119 μm in the lateral direction, 86 μm in the axial direction, and 1.2 mm in the elevational direction [17].

In our PA elastography system, an aluminum compression plate larger than the object exerted a small axial compressive force on the object [Fig. 1(a)]. An imaging window slightly larger than the ultrasonic transducer probe was opened at the center of the compression plate [Fig. 1(b)]. A piece of fully stretched polymethylpentene (TPX) plastic membrane was attached to the bottom of the compression plate to provide uniform and uniaxial force to the object while passing the illumination laser beam. Ultrasound gel was used for acoustic coupling between the compression plate and the object without changing the elasticity of the gelatin phantoms. Ultrasound gel is also convenient for *in vivo* animal imaging and potential clinical applications. For acoustic coupling between the probe and the compression plate, water was chosen as the medium. The compression plate was adjusted by a manual translation stage to provide precise compression to the object against a rigid object holder. The total displacement of the object surface was

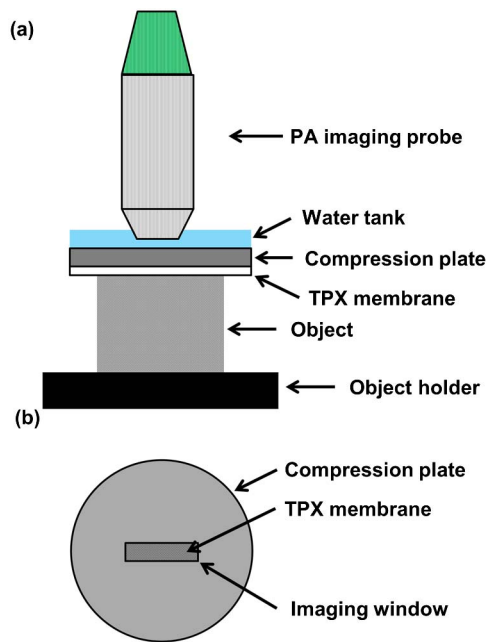


Fig. 1. Schematic of the PA elastography system: (a) side view of the PA elastography system and (b) top view of the compression plate with the imaging window at the center.

read from the translation stage. The object and the object holder were placed on a high-precision digital weighing scale (S200, Ohaus). The compression stress applied to the object was calculated from the difference in the scale readings before and after compression

$$\sigma = \frac{g(m_a - m_b)}{A}. \quad (1)$$

Here, σ is the compression stress, g is the acceleration of gravity, m_a and m_b are the scale readings before and after compression, and A is the area on which the compression force is applied.

To demonstrate quantitative elasticity measurement, PA elastography was first used to image four homogeneous gelatin phantoms with respective gelatin concentration of 40, 60, 80, and 100 g/L. To provide absorption contrast for PA imaging, 50 μm microspheres were mixed in the gelatin phantoms at a concentration of ~ 5 microspheres per mm^3 . Each gelatin phantom was imaged with the PA elastography system before and after compression with an external stress of 53 Pa [Figs. 2(a) and 2(b)]. The maximum surface displacement in the experiments was 120 μm , and the maximum strain was 4%, which was considered to be within the linear strain response regime of the phantom [18]. Time-resolved A-line signals before and after compression were cross-correlated to calculate the axial displacement due to compression [19], generating a cross-sectional map of displacements after compression [Fig. 2(c)]. Here, short-window cross-correlation between corresponding A-lines was computed. We slid a 90- μm -wide window along the A-lines acquired before and after compression, and computed the cross-correlations to find the displacement between the A-lines at each window position. Displacements were then averaged among the microspheres at each depth [Fig. 2(d)]. The slope of the linear fitting of the displacements versus depths—i.e., the magnitude of the average gradient of the

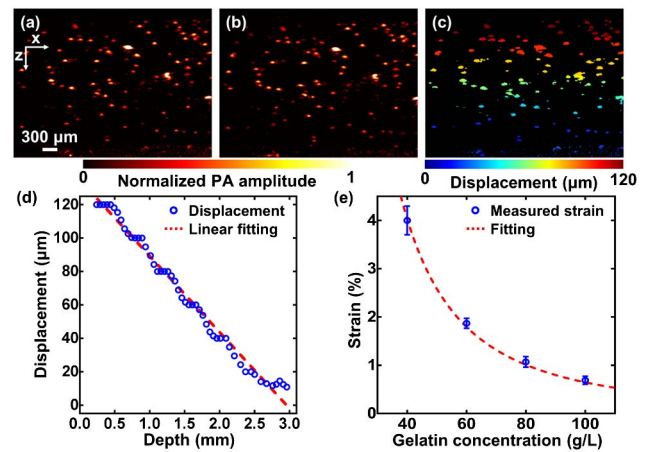


Fig. 2. Strain measurement on single-layer gelatin phantoms by PA elastography: (a) and (b) cross-sectional PA images of a gelatin phantom (40 g/L gelatin concentration) mixed with 50 μm microspheres acquired (a) before and (b) after compression; (c) displacement image obtained from (a) and (b); (d) average displacement versus the depth. The strain of the phantom was estimated as the slope of the linear fitting. (e) Measured strains of gelatin phantoms with 4%, 6%, 8%, and 10% concentration in weight. The data was fitted to a quadratic model that describes the relationship between the strain and the gelatin concentration [Eq. (2)].

displacement—quantified the average strain of each gelatin phantom. The same data processing was performed on 20 measurements, five each for four gelatin phantoms [Fig. 2(e)]. The measured strains were then fitted by the model below [18]

$$\varepsilon = \frac{\sigma}{K} \frac{1}{C^2}. \quad (2)$$

Here, ε is the strain of the gelatin phantom, σ is the stress applied to the phantom, K is a constant factor, and C is the gelatin concentration. Note K is affected by the equilibrium temperature, the temperature and duration of the gelatin mixing process, and the molecular weight of gelatin.

PA elastography was then used to image a bilayer gelatin phantom with different gelatin concentrations in each layer. The top layer had a gelatin concentration of 50 g/L and a thickness of 2.5 mm. The bottom layer had a gelatin concentration of 100 g/L and a thickness of 2.0 mm. Again, 50 μm microspheres were mixed in the gelatin phantom at the concentration of 5 microspheres per mm^3 . The bilayer phantom was imaged by the PA elastography system before and after compression with a stress of 98 Pa [Figs. 3(a) and 3(b)]. A displacement image was generated using the same method as above [Fig. 3(c)]. Displacements of the microspheres were averaged at each depth and fitted by a linear function for each layer [Fig. 3(d)]. The slopes of the two linear fittings reflect the strains in the two layers. The strain ratio between the two layers is 4.0 ± 0.2 , which agrees with the theoretical value of 4.

A mouse leg was then imaged *in vivo* by PA elastography. All experimental animal procedures were carried out in conformity with laboratory animal protocols approved by the Animal Studies Committee at Washington University in St. Louis. The mouse leg was imaged before and after applying an external compression force of 12 mN [Figs. 4(a) and 4(b)]. A displacement image was obtained by cross-correlating the PA images

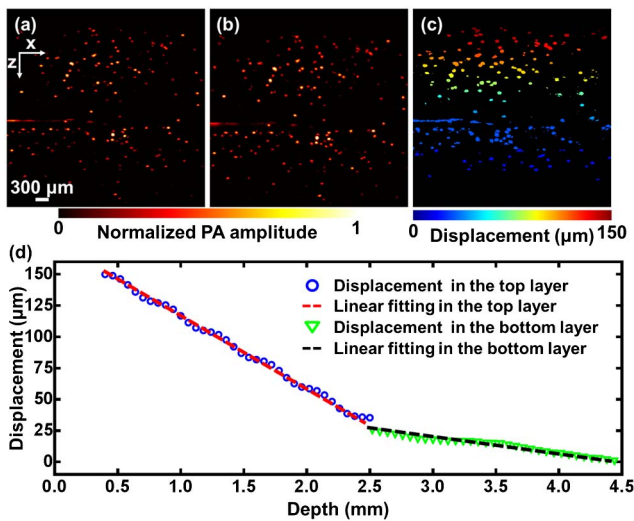


Fig. 3. Strain measurement of a bilayer gelatin phantom by PA elastography: (a) and (b) PA images of a bilayer gelatin phantom mixed with 50 μm microspheres acquired (a) before and (b) after compression; (c) displacement image obtained from (a) and (b); (d) average displacement versus depth. The data was fitted by a linear function for each layer.

before and after compression, using the image pixels with PA signal amplitudes above the noise level. A raw strain image was then obtained by numerically differentiating the axial displacements, assuming that the applied stress was uniaxial [Fig. 4(c)]. The raw strain image was then superimposed on the structural PA image [Fig. 4(e)]. The regions of tissue with larger strains were softer than regions with smaller strains, and thus were thought to have more fat. The PA elastography was validated by ultrasound elastography using the same linear-array imaging probe, which showed a similar distribution of strains [Figs. 4(d) and 4(f)]. In ultrasound elastography, structural ultrasound images were acquired simultaneously with structural PA images

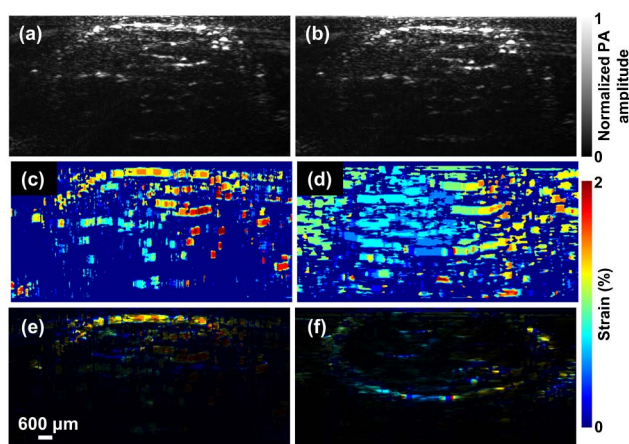


Fig. 4. PA elastography of a mouse leg *in vivo*. (a) and (b) PA images of a mouse leg *in vivo* before and after compression, (c) strain image of the mouse leg obtained by PA elastography *in vivo*, (d) strain image of the mouse leg obtained by ultrasound elastography *in vivo*, (e) strain image of the mouse leg obtained by PA elastography superimposed on the structural PA image, and (f) strain image of the mouse leg obtained by ultrasound elastography on the structural ultrasound image.

before and after compression. The displacement and strain images in the ultrasound elastography were computed using the same data processing method as in the PA elastography. The average strains over the entire cross-sectional image were $0.84 \pm 0.49\%$ in PA elastography and $0.82 \pm 0.29\%$ in ultrasound elastography. Here it is worth noting that there were differences between the strain distribution measured by PA elastography and ultrasound elastography. Although both methods measured the elastic property of the tissue, they were based on different contrast mechanisms. Within each resolution voxel ($\sim 119 \mu\text{m}$ by $86 \mu\text{m}$ by 1.2mm) of the strain image, optical-absorption-based PA elastography measured the integrated elasticity of the tissue only through the displacement of the vasculature, while acoustic-scattering-based ultrasound elastography mapped the integrated elasticity through the displacement of more tissue components, including vasculature, muscle fibers, and fat. Under compression, there may be more relative displacements between vasculature and other tissue components in the soft regions, resulting in higher strain values than those in ultrasound elastography. Another possible reason for the discrepancy between the measured strain images is the different number of useful pixels in PA and ultrasound elastography images. Lacking speckles, and imaging only the blood vasculature, PA elastography has fewer useful pixels than ultrasound elastography, resulting in fewer effective pixels for interpolation, especially in the tissue region with less blood.

Compared to previous studies, our PA elastography technique based on a linear-array PACT has the following distinctive features [12–15]: first, PA elastography maps the Young's modulus of biological tissue, but previous PA viscoelasticity studies are based on the contrast of the viscosity-elasticity ratio [12,13]; second, PA elastography is able to provide cross-sectional strain images of biological tissue with high axial resolution, while viscosity-elasticity ratio measurement has no axial resolution [12,13]; third, PA viscoelasticity imaging is based on an intensity-modulated CW laser excitation, yielding a much lower signal-to-noise ratio than that in PA elastography using a pulsed laser excitation [20]; fourth, PA elastography is implemented on a commercial linear-array-based PACT system, which can measure other biological parameters including vasculature density, tumor volume, oxygen saturation of hemoglobin, and blood flow velocity [16,17,21].

In summary, we have demonstrated PA elastography on gelatin phantoms and *in vivo*. Lacking speckles, PA elastography can still measure tissue displacements using optical absorption contrast provided by abundant endogenous biomolecules, especially hemoglobin in red blood cells [22]. PA elastography has a 100% relative sensitivity to optical absorption contrast, which means a given percentage change in the optical absorption coefficient yields the same percentage change in the PA signal amplitude. PA elastography is well suited for mapping the elastic properties of diseased tissues with highly vascularized structures, such as carcinoma and glioblastoma [23]. At longer wavelengths, where water and lipids have relatively strong absorption, PA elastography can potentially map the elastic properties of tissues by using water and lipids as the contrast [24,25].

We would like to point out that the motivation for this Letter is not to prove that PA elastography is superior to ultrasound elastography. Instead, the major motivation is to demonstrate the feasibility of elasticity measurement by using

PAT as an independent device: not all the PA imaging systems have the capability of ultrasound transmission, and thus ultrasound elastography is not always available. PA elastography can be implemented on existing PA imaging systems, as an additional function, to provide more comprehensive information about the tissue's mechanical and functional information.

Further, PAT can potentially measure elasticity concurrently with other functional parameters, including the oxygen saturation of hemoglobin, which may provide more comprehensive information for disease diagnosis and treatment evaluation [26]. Noninvasive imaging of elasticity distribution expands the functionality of PAT and is expected to find potential applications in clinical practice, such as cancer detection and arterial plaque assessment. To advance the current PA elastography technique for clinical applications, several challenges remain to be solved. One challenge is to apply normal uniform compression force *in vivo*. A special compression mechanism needs to be developed for curved tissue surfaces. Another challenge is to achieve 3D volumetric strain imaging. To achieve this, the current linear-array PA probe can be linearly scanned orthogonally.

Funding. National Institutes of Health (NIH) (DP1-EB016986, R01-CA186567, S10-RR026922); March of Dimes Foundation (22FY14486).

Acknowledgment. The authors appreciate Prof. James Ballard's close reading of the manuscript. L. V. Wang has a financial interest in Endra, Inc., and Microphotoacoustics, Inc., which, however, did not support this work.

REFERENCES

1. J. F. Greenleaf, M. Fatemi, and M. Insana, *Annu. Rev. Biomed. Eng.* **5**, 57 (2003).
2. L. Gao, K. J. Parker, R. M. Lerner, and S. F. Levinson, *Ultrasound Med. Biol.* **22**, 959 (1996).
3. J. Ophir, S. K. Alam, B. S. Garra, F. Kallel, E. E. Konofagou, T. Krouskop, C. R. B. Merritt, R. Righetti, R. Souchon, S. Srinivasan, and T. Varghese, *J. Med. Ultrasonics* **29**, 155 (2002).
4. J. Ophir, I. Céspedes, H. Ponnekanti, Y. Yazdi, and X. Li, *Ultrason. Im.* **13**, 111 (1991).
5. A. Manduca, T. E. Oliphant, M. A. Dresner, J. L. Mahowald, S. A. Kruse, E. Amromin, J. P. Felmlee, J. F. Greenleaf, and R. L. Ehman, *Med. Image Anal.* **5**, 237 (2001).
6. C. Sun, B. Standish, and V. X. D. Yang, *J. Biomed. Opt.* **16**, 043001 (2011).
7. L. V. Wang and S. Hu, *Science* **335**, 1458 (2012).
8. L. V. Wang, *Nat. Photonics* **3**, 503 (2009).
9. X. Wang, Y. Pang, G. Ku, X. Xie, G. Stoica, and L. V. Wang, *Nat. Biotechnol.* **21**, 803 (2003).
10. P. Hai, J. Yao, K. I. Maslov, Y. Zhou, and L. V. Wang, *Opt. Lett.* **39**, 5192 (2014).
11. L. V. Wang and L. Gao, *Annu. Rev. Biomed. Eng.* **16**, 155 (2014).
12. G. Gao, S. H. Yang, and D. Xing, *Opt. Lett.* **36**, 3341 (2011).
13. Y. Zhao, S. Yang, C. Chen, and D. Xing, *Opt. Lett.* **39**, 2565 (2014).
14. N. Wadamori, *Appl. Phys. Lett.* **105**, 103707 (2014).
15. T. Glatz, O. Scherzer, and T. Widlak, *J. Math. Imaging Vision* **52**(3), 369 (2014).
16. A. Needles, A. Heinmiller, J. Sun, C. Theodoropoulos, D. Bates, D. Hirson, M. Yin, and F. S. Foster, *IEEE Trans. Ultrason. Ferroelectr. Freq. Control* **60**, 888 (2013).
17. Y. Zhou, G. Li, L. Zhu, C. Li, L. A. Cornelius, and L. V. Wang, *J. Biophoton.* **1**, 7 (2015).
18. T. Hall, M. Bilgen, M. Insana, and T. Krouskop, *IEEE Trans. Ultrason. Ferroelectr. Freq. Control* **44**, 1355 (1997).
19. J. M. Schmitt, *Opt. Express* **3**, 199 (1998).
20. K. Maslov and L. V. Wang, *J. Biomed. Opt.* **13**, 024006 (2008).
21. Y. Zhou, J. Liang, and L. V. Wang, *J. Biophoton.*, doi: 10.1002/jbio.201500181 (to be published).
22. Z. Guo, L. Li, and L. V. Wang, *Med. Phys.* **36**, 4084 (2009).
23. J. Yao and L. V. Wang, *Photoacoustics* **2**, 87 (2014).
24. Z. Xu, C. H. Li, and L. V. Wang, *J. Biomed. Opt.* **15**, 036019 (2010).
25. T. Matthews, C. Zhang, D. Yao, K. Maslov, and L. V. Wang, *J. Biomed. Opt.* **19**, 016004 (2014).
26. J. Yao, L. Wang, J. M. Yang, K. I. Maslov, T. T. Wong, L. Li, C. H. Huang, J. Zou, and L. V. Wang, *Nat. Methods* **12**, 407 (2015).